Unveiling the Synergistic Effect of Two-Dimensional Heterostructure NiFeP@FeOOH as Stable Electrocatalyst for Oxygen Evolution Reaction

Qinglong Hou [1,†], Zhigang Jiang [1,†], Chen Wang [1], Shuhan Yang [1], Haizhen Liu [2], Bo Xing [3,*], Honghui Cheng [4] and Kuikui Wang [1,5,*]

1   Institute of Materials for Energy and Environment, Laboratory of New Fiber Materials and Modern Textile, Growing Basis for State Key Laboratory, College of Materials Science and Engineering, Qingdao University, Qingdao 266071, China; houqinglong7125@163.com (Q.H.); q554469885@163.com (Z.J.); wc06290643@163.com (C.W.); 17860757252@163.com (S.Y.)
2   MOE Key Laboratory of New Processing Technology for Non-ferrous Metals and Materials, Guangxi Key Laboratory of Processing for Non-ferrous Metals and Featured Materials, Guangxi University, Nanning 530004, China; liuhz@gxu.edu.cn
3   National Engineering Laboratory of Circular Economy, Sichuan University of Science and Engineering, Zigong 643000, China
4   School of Mechanical Engineering, Yangzhou University, Yangzhou 225127, China; hhcheng@yzu.edu.cn
5   Jiangsu Key Laboratory of Advanced Catalytic Materials and Technology, Changzhou University, Changzhou 213164, China
*   Correspondence: xingbo0216@163.com (B.X.); kkwang@qdu.edu.cn (K.W.)
†   These authors contributed equally to this work.

Abstract: Introducing multiple active sites and constructing a heterostructure are efficient strategies to develop high-performance electrocatalysts. Herein, two-dimensional heterostructure NiFeP@FeOOH nanosheets supported by nickel foam (NF) are prepared by a hydrothermal–phosphorization–electrodeposition process. The synthesis of self-supporting heterostructure NiFeP@FeOOH nanosheets on NF increases the specific surface region, while bimetallic phosphide realizes rapid charge transfer, improving the electron transfer rate. The introduction of FeOOH and the construction of a heterostructure result in a synergistic effect among the components, and the surface-active sites are abundant. In situ Raman spectroscopy showed that the excellent oxygen evolution reaction (OER) performance was due to reconstruction-induced hydroxyl oxide, which achieved a multi-active site reaction. The NiFeP@FeOOH/NF electrocatalytic activity was then significantly improved. The findings indicate that in a 1.0 M KOH alkaline solution, NiFeP@FeOOH/NF showed an OER overpotential of 235 mV at 100 mA cm^{-2}, a Tafel slope of 46.46 mV dec^{-1}, and it worked stably at 50 mA cm^{-2} for 80 h. This research proves that constructing heterostructure and introducing FeOOH are of great significance to the study of the properties of OER electrocatalysts.

Keywords: heterostructure; nanosheet; FeOOH; stability; oxygen evolution reaction

1. Introduction

Studying and developing green and sustainable energy is becoming increasingly important as energy and environmental problems become worse [1,2]. Hydrogen is an excellent replacement for fossil fuels as it has a high energy density and creates zero emissions [3,4]. Sustainable hydrolysis to produce hydrogen will be the future direction of energy development [5,6]. For large-scale industrial production, the efficiency of electrolyzed water energy conversion is insufficient, so it is critical to investigate and develop high-performance electrolyzed water catalysts [7,8]. In reality, the voltage needed for the hydrolysis reaction is greater than the theoretical voltage [9–12]. The OER under alkaline conditions is a four-electron coupling reaction. Because of its slow reaction kinetics, the real

efficiency of electrolytic water is extraordinarily low [13]. IrO_2/RuO_2 is the standard OER catalyst commonly used now [14–17]. However, owing to the rarity of expensive metal materials, it is difficult to sustain it in large-scale industrial production and application for an extended period [18,19]. As a result, the creation of non-precious metal catalysts with elevated electrolysis productivity and low cost holds critical research value [20,21].

In an attempt to develop electrocatalyst materials, many scientists have focused on transition metal materials (such as nickel, cobalt, iron, etc.). Many transition metal-based compounds have been developed up to this point [22]. Researchers are particularly intrigued with transition metal phosphides because of their notably high mechanical strength, conductivity, and chemical stability [23]. Nickel–iron-based phosphide is considered to be an effective material for OER catalyst, because the interaction between Fe^{3+} and Ni^{2+} can alter the electron density distribution or electronic structure of the catalyst [24–27]. However, given the current need for commercial water electrolysis, increasing nickel–iron-based phosphide catalytic activity and stability is necessary.

Currently, it is possible to increase catalytic activity by altering the electronic arrangement to increase the strength of intermediate adsorption at active sites [28,29]. The main methods include heterojunction construction, interface modification, defect engineering, and strain adjustment [30]. Among these methods, creating heterojunctions can greatly enhance the catalyst catalytic efficiency. A reasonable interface heterostructure design can modify electroactive sites, facilitate electron transfer, enhance the synergistic effect of each component, and improve catalytic activity as well as optimize intermediate adsorption energy [31]. Furthermore, charge transfers in the catalytic process can be facilitated by the heterojunction catalyst's built-in electric field, which improves the kinetics of the electrode reaction. According to Jin et al., creating heterostructures can significantly enhance OER catalyst performance [32]. Zhao et al. created a high-performance OER catalyst via building a heterostructure [33]. Wu et al. used the synergistic effect between two different nickel–iron-based materials to prepare NiFe-OH/NiFeP materials with excellent OER properties [34]. As a result, designing and building heterojunctions is an extremely significant way for improving the electrocatalytic performance of electrocatalysts.

Numerous studies have demonstrated that FeOOH is the most catalytically active component of iron-based OER catalysts in alkaline solutions [34,35]. FeOOH has risen in popularity and has become a crucial component of OER catalysts because of its strong inherent activity and unique D-electron structure [36]. However, single FeOOH has poor conductivity, excessive intermediate adsorption energy, and an unstable structure, while transition metal phosphide offers high physical strength, conductivity, and stability, so the synergistic effect of transition metal phosphide combined with FeOOH may substantially enhance the electrocatalytic activity of the catalysts. Zhang et al. demonstrated that inserting FeOOH improves the OER electrocatalytic activity of $Ni_2P/FeOOH$ [37]. Gao et al. increased the OER activity of the samples by including FeOOH [38].

Based on the earlier work, herein, we designed the 2D heterostructure NiFeP@FeOOH nanosheets based on NF for OER electrocatalysts. The synthesized NiFeP@FeOOH/NF exhibits increased electrocatalytic performance. The OER overpotential required for the NiFeP@FeOOH/NF catalyst to accomplish a current density of 100 mA cm^{-2} is 235 mV in 1.0 M KOH solution. The nickel foam substrate in NiFeP@FeOOH/NF has an open structure and high specific surface area, and the bimetallic phosphide can realize rapid charge transfer. The construction of heterogeneous structures and the introduction of FeOOH increase the number of active sites on the surface and enhance the synergistic effects. Therefore, by constructing a heterojunction and introducing FeOOH, the OER performance can be significantly increased. This transition metal phosphide design technique has the potential to increase the performance of OER electrocatalysts.

2. Results and Discussion

As seen in Figure 1a, the NiFeP@FeOOH/NF OER electrocatalyst was designed and synthesized on NF by the hydrothermal–phosphorization–electrodeposition method. First,

a straightforward hydrothermal method was used for the in situ generation of Ni-Fe bimetallic hydroxide on nickel foam. The surface of NF was flat and smooth, and under a high-power scanning electron microscope, it resembles scales as seen in Figure S1. The Ni-Fe bimetallic hydroxide grows vertically on the surface of NF, resulting in two-dimensional nano-sheets interwoven with each other as seen in Figure 1b. As seen in Figure 1c, the two-dimensional nano-flake structure on the surface rarely changes after gas phase phosphating, and this shows that the steps of phosphating have not much of an impact on the morphology of the sample. Compared with Ni_2P/NF, the nano-flake surface of NiFeP/NF has obvious granular protrusions after phosphating Ni_2P/NF in Figure S2, which implies that the introduction of Fe element into the precursor is beneficial to maintaining the nano-flake structure. After a constant current deposition, FeOOH nanosheets grow evenly on NiFeP surface as shown in Figure 1d. Additionally, we confirmed that the FeOOH nanosheets could be successfully grown by electrodeposition on the surface of NF by comparing the SEM images of the FeOOH/NF (Figure S3). Shell-like aggregation can be easily seen on the surface of FeOOH/NF in comparison to the SEM images of NiFeP@FeOOH/NF. It shows that electrodeposition of FeOOH on NiFeP nanosheets is beneficial to regular growth and inhibition of its aggregation. It is possible to investigate the Ni, Fe, O, and P elements evenly distributed on the NiFeP@FeOOH/NF surface detection area through scanning electron microscope (SEM) elemental analysis. According to Figure 1e–i, the elemental mapping also demonstrates that the sample surface was successfully phosphatized and grew FeOOH by vapor phase phosphating and electrodeposition. In addition, as shown in Figure S4, to obtain NiFe precursor with uniform distribution of nanosheets, the formation of nanosheets was controlled by controlling the hydrothermal temperature. Under the condition of 120 °C, the distribution of nanosheets on the surface of the NiFe precursor was the most uniform. This facilitated the implementation of the subsequent steps to achieve synergies between the components. Through the above steps, we successfully obtained the heterostructure NiFeP@FeOOH nanosheets. Nitrogen adsorption/desorption isotherms were measured, and the specific surface areas of the NiFe precursor/NF and NiFeP@FeOOH/NF were estimated to be 35.25 m^2 g^{-1} and 37.62 m^2 g^{-1} based on the Brunauer–Emmtt–Teller (BET) model.
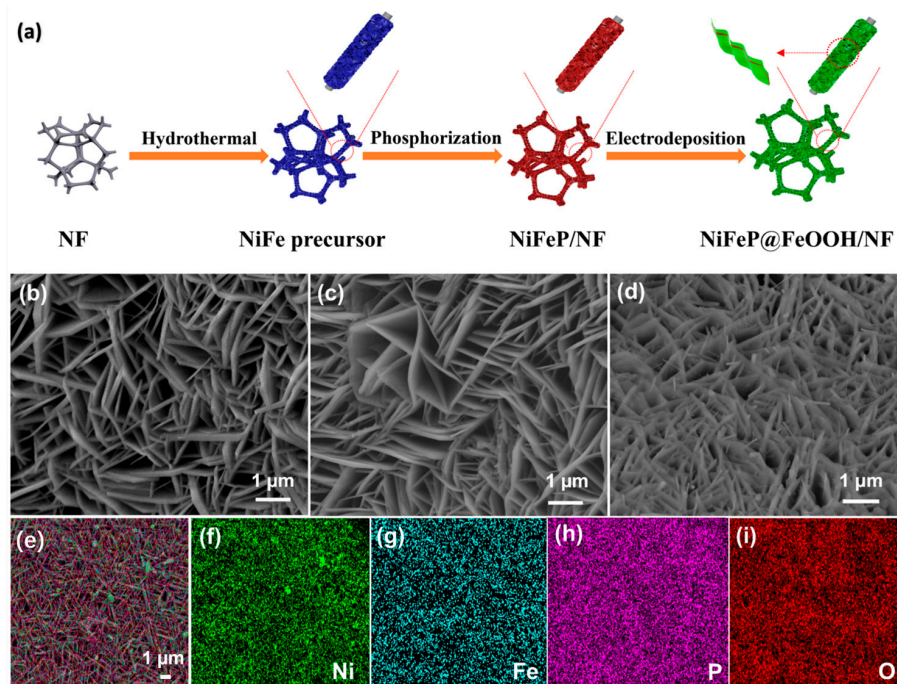

Figure 1. (**a**) Scheme of the preparation of NiFeP@FeOOH/NF, SEM images of (**b**) NiFe precursor, (**c**) NiFeP/NF, and (**d**) NiFeP@FeOOH/NF, (**e**–**i**) Elemental mapping images of the NiFeP@FeOOH/NF.

Transmission electron microscopy (TEM) was used to further research the structure and content of NiFeP@FeOOH/NF (Figure 2a–g), along with scanning electron microscope (SEM) elemental analysis (Figure 2h). Figure 2a,b show that the NiFeP@FeOOH nanosheet is in two dimensions, which demonstrates that the nanosheet is composed of lots of crystalline nanoparticles. The SEM images support this as well. As seen in Figure 2c, the two-dimensional NiFeP@FeOOH nanosheets are further enlarged, and the TEM of the high-resolution (HRTEM) images show three groups of clear lattice stripes, which correspond to Figure 2d–f, respectively. The measured crystal plane spacings of 0.29 nm, 0.22 nm, and 0.25 nm match the crystal planes of Fe_2P (101), Ni_2P (111), and FeOOH (211), respectively. The findings show that Fe_2P, Ni_2P, and FeOOH make up the NiFeP@FeOOH nanosheets, and that there is a clear interface boundary between them as shown in Figure 2g. This indicates that the NiFeP@FeOOH heterostructure has been successfully constructed. This heterostructure helps to regulate electron transport and speeds up the intermediate adsorption and desorption during electrocatalytic reactions. At the same time, the synergistic effect between the components is improved, enhancing the catalytic performance. In addition, transmission analysis was performed on multiple regions of the sample, and there were also heterostructures, as shown in Figure S5. A series of diffraction rings with numerous bright spots can be seen in Figure 2h (the selective electron diffraction (SAED) image), which displays the crystal planes of Fe_2P (101), Ni_2P (111), and FeOOH (211). Additionally, the experimental NiFeP@FeOOH/NF contact angle was measured, as can be seen in Figure S6, and the contact angle was 46.3°, indicating that the sample had good hydrophilicity. Better wettability can improve the interaction between catalyst and electrolyte, exposing more active sites to the catalyst. From the above results, it can be seen that the preparation of heterogeneous NiFeP@FeOOH nanosheets was successful, and it may show advantageous OER activity through multi-component synergism.
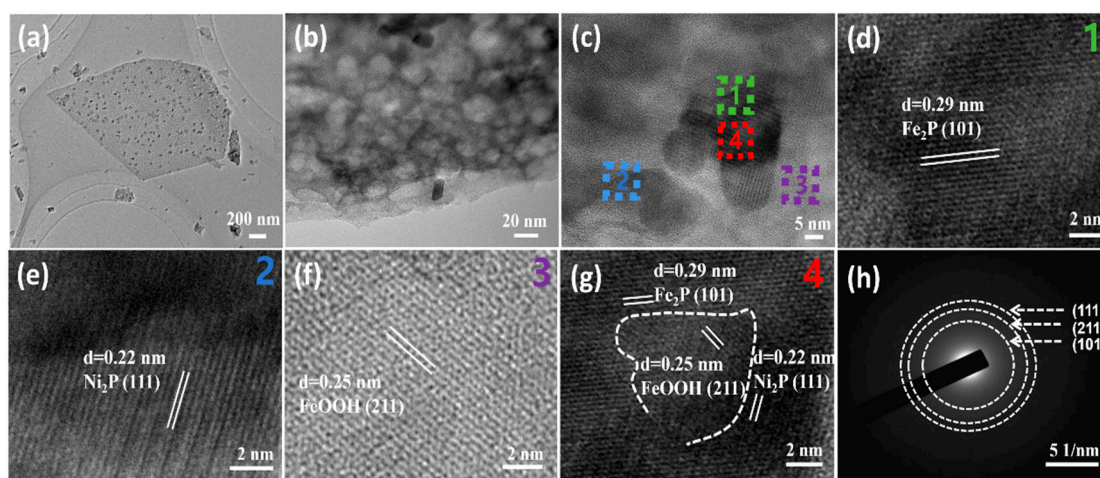

Figure 2. (**a**–**g**) HRTEM images of the NiFeP@FeOOH/NF, (**h**) SAED image of NiFeP@FeOOH/NF.

The chemical composition of NiFeP@FeOOH/NF was further examined using X-ray diffraction (XRD) and X-ray photoelectron spectroscopy (XPS). The crystal structure of the resulting electrocatalyst was examined by X-ray diffraction (XRD). According to Figure 3a, the three most obvious diffraction peaks are located at 76.5°, 52.0°, and 44.6°, which are mainly attributed to Ni (PDF#04-0850). Apart from these, the additional diffraction peaks are Ni_2P (PDF#03-0953), Fe_2P (PDF#51-0943), and FeOOH (PDF#46-1315), respectively [10,37]. NiFeP/NF is a combination of Ni_2P and Fe_2P. After the introduction of FeOOH, there is no obvious peak generation or shift in NiFeP@FeOOH/NF. This shows that FeOOH grown by electrodeposition has poor crystallinity. Their chemistry composition and valence were further analyzed using XPS. The entire spectrum depicted in Figure 3b establishes the presence of Ni, Fe, O, C and P elements in the NiFeP@FeOOH/NF sample. Indicating in Figure 4, high-resolution spectra of NiFeP/NF were used to compare

the changes in binding energy peaks after the introduction of FeOOH. Figure 4a depicts the full spectrum of the NiFe precursor, and the full spectrum of NiFeP/NF is obtained after phosphating (Figure 4b). Four distinctive peaks and two adjoint peaks can be seen in the spectrum of high-resolution Ni 2p (Figure 3c). Among them, the two binding energy peaks of Ni $2p_{1/2}$ and Ni $2p_{3/2}$ of Ni-O are at 874.3 eV and 856.3 eV, respectively. The binding energy peaks at 872.0 eV and 853.8 eV associated with Ni-P [39,40]. The two satellite peaks are at 861.0 eV and 879.6 eV, respectively. Compared with Figure 4c, the introduction of FeOOH redistributes the electron density, resulting to a positive shift of the Ni–P bond peak by 0.5 eV. The binding energies are also shown in Table S1.
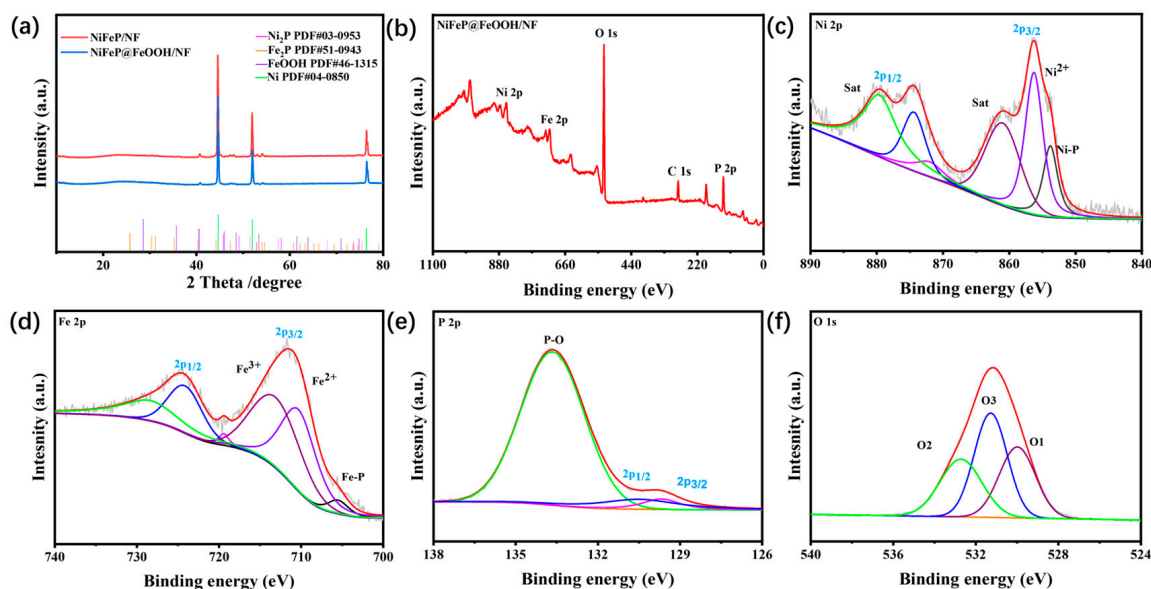

Figure 3. (**a**) XRD patterns of NiFeP/NF and NiFeP@FeOOH/NF High-resolution fitted, (**b**) Survey XPS spectrum of NiFeP@FeOOH/NF and high-resolution spectra of (**c**) Ni 2p, (**d**) Fe 2p, (**e**) P 2p, and (**f**) O 1s.
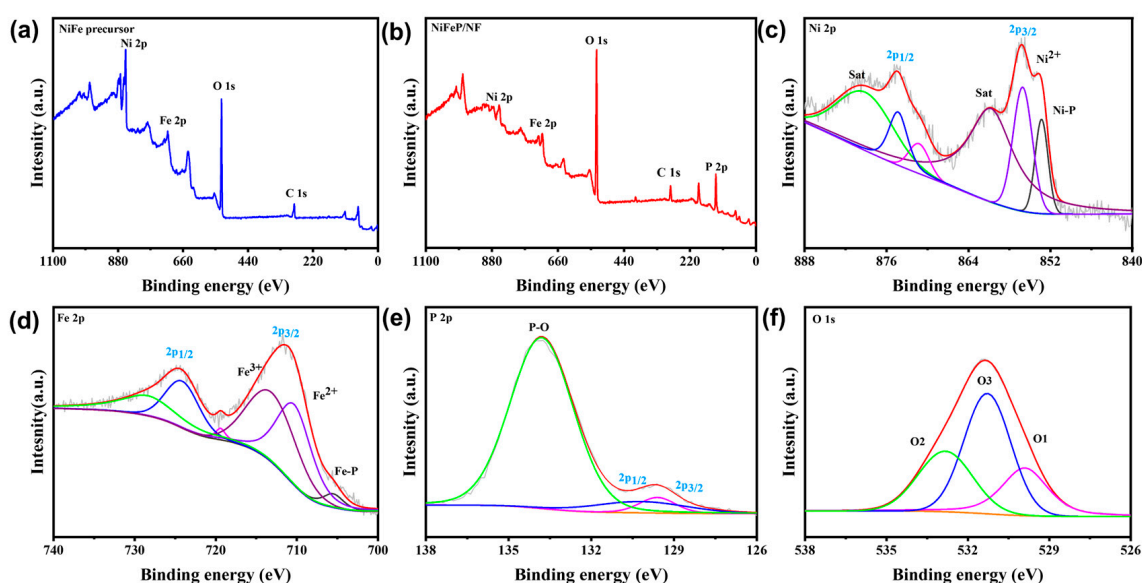

Figure 4. (**a**) Full spectrum of NiFe precursor, (**b**) Survey XPS spectrum of NiFeP/NF and high-resolution spectra of (**c**) Ni 2p, (**d**) Fe 2p, (**e**) P 2p, and (**f**) O 1s.

The XPS spectra of Fe 2p in NiFeP@FeOOH/NF are displayed in Figure 3d. Peaks in the binding energy at 705.4 eV and 719.4 eV belong to Fe-P. The second and third peaks

in the binding energy of Fe $2p_{3/2}$ and Fe $2p_{1/2}$ appear at 710.3 eV, 724.1 eV, and 713.1 eV, 728.4 eV, belonging to Fe^{2+} and Fe^{3+}, respectively [34]. After introducing FeOOH, the content of Fe increases greatly compared with Figure 4d, and the area of Fe^{3+} diffraction peak is increased. Figure 3e is the spectrum of P 2p. Metal phosphides are responsible for the two binding energy peaks at 129.7 eV and 130.5 eV, respectively. The binding energy of P-O peaks at 133.6 eV, which is due to the catalyst oxidization when it comes into contact with airborne oxygen [41,42]. As seen in Figure 4e, the binding energy peak of P did not change greatly after the introduction of FeOOH. Figure 3f displays the O 1 s spectrum, in which there are three binding energy peaks. They belong to the M-O (530.0 eV), M-OH (531.3 eV), and adsorbed H_2O (532.7 eV) sections, respectively [26,43]. The peak of NiFeP@FeOOH/NF O1s is negatively shifted by 0.1 eV compared with NiFeP/NF (Figure 4f), indicating that the electron density is enhanced after the introduction of FeOOH. The XPS data further demonstrate the generation of FeOOH and a significant number of OH groups. This improves the internal activity of the catalyst by changing the local electron arrangement and speeding up electron transport.

A conventional three-electrode setup was used for testing the electrocatalytic OER performance of NiFeP@FeOOH/NF in a 1.0 M KOH electrolyzer. The same conditions were used for testing NF, Ni_2P@FeOOH/NF, NiFeP/NF, FeOOH/NF, and RuO_2/NF. Apart from comparing the OER performance of the precursor and NiFeP@FeOOH/NF, the LSV curves of NiFeP@FeOOH/NF and other materials are displayed in Figure 5a. Among these catalysts, NiFeP@FeOOH/NF displays the highest OER activity. Due to the existence of metal oxidation peak, the metal is polarized under the influence of current, resulting in potential deviation from low state to high state [44,45]. Reverse scanning is utilized to reduce the impact of metal oxidation peaks at 100 mA cm^{-2}. In order to make a comparison, the overpotential at a current density of 100 mA cm^{-2} is extracted and depicted as a bar graph in Figure 5b. In comparison to other materials, NiFeP@FeOOH/NF requires a 235 mV overpotential under a current density of 100 mA cm^{-2}. According to the data, the NiFeP@FeOOH exhibits excellent electrocatalytic performance. After phosphatization and electrodeposition of the precursor, the OER performance of NiFeP@FeOOH/NF is considerably improved as appears in Figure S7. This demonstrates that the construction of heterojunctions and the introduction of FeOOH enhance the synergistic effects among the components and increase the catalytic activity of NiFeP@FeOOH/NF.

The Tafel diagram and EIS spectrum were further employed to demonstrate the kinetic characteristics of OER. According to Figure 5c, the Tafel slope of NiFeP@FeOOH/NF is 46.46 mV dec^{-1}, which is lower than Ni_2P@FeOOH/NF (63.31 mV dec^{-1}), NiFeP/NF (74.25 mV dec^{-1}), RuO_2/NF (121.27 mV dec^{-1}), and bare NF (166.79 mV dec^{-1}). This demonstrates that NiFeP@FeOOH/NF has excellent OER reaction kinetics. Moreover, EIS spectroscopy is frequently utilized in the OER process to understand charge transfer behavior and interfacial reaction features. All samples were examined at a voltage of 100 mA cm^{-2} in Figure 5d. The NiFeP@FeOOH/NF exhibits a little semicircle. Following simulation using an equivalent circuit in a Nyquist plot, R_{ct} was determined to be 0.9 Ω at the zone of high frequency, which is the smallest compared to other materials. R_{ct} (Ni_2P@FeOOH/NF) is 1.0 Ω, R_{ct} (NiFeP/NF) is 1.1 Ω, R_{ct} (FeOOH/NF) is 1.9 Ω, R_{ct} (RuO_2/NF) is 6.0 Ω, and R_{ct} (NF) is 2.4 Ω, indicating that electron transport in the NiFeP@FeOOH/NF electrode is faster, which leads to higher OER catalytic performance. This is due to the fact that the constructed two-dimensional heterostructure can increase the rate of electron transfer and accelerate the rate of bubble release thus speeding up the reaction rate. Comparing the OER catalytic properties of NiFeP@FeOOH/NF with those of NiFeP/NF and Ni_2P@FeOOH, the multi-component synergistic action of NiFeP@FeOOH/NF shows the best catalytic performance. We performed in situ Raman analysis using three-electrode cells to further explore the structural evolution during the electrochemical process. Figure 5e shows the curves of a series of Raman spectra of NiFeP@FeOOH/NF immersed in 1.0 M KOH with an applied potential. Before the application of potential, the Raman spectrum of NiFeP@FeOOH/NF had a peak at 696.0 cm^{-1}, which can be attributed to the FeOOH

obtained by electrodeposition. When a potential is applied to the electrode, the peak becomes stronger, and its strength initially increases as the applied potential increases. Meanwhile, the peaks produced at 480.0 cm^{-1} and 567.0 cm^{-1} are attributed to NiOOH, and their intensity increases with the increase in applied potential [15]. The results show that a large amount of hydroxyl radical is produced during the catalytic reaction, which are the most active components in the catalytic process of the OER reaction, consistent with the previous literature reports. NiFeP@FeOOH/NF has an outstanding OER performance, as shown in Figure 5f, compared to a variety of Fe and Ni-based OER catalysts. Table S2 compares the performance of NiFeP@FeOOH with other OER catalysts. Additionally, the surface morphology of the samples was regulated by adjusting the electrodeposition time, and the best electrodeposition time was discovered (Figure S8). It was discovered that the OER performance of samples was highest when electrodeposition was performed for 100 s. Because the electrodeposition time is too long, there will be particle aggregation on the sample surface, which will affect the synergy between the components and thus affect the electrocatalytic performance (Figure S9). Conversely, when the electrodeposition time is too short, FeOOH nanosheets are not equally covered.
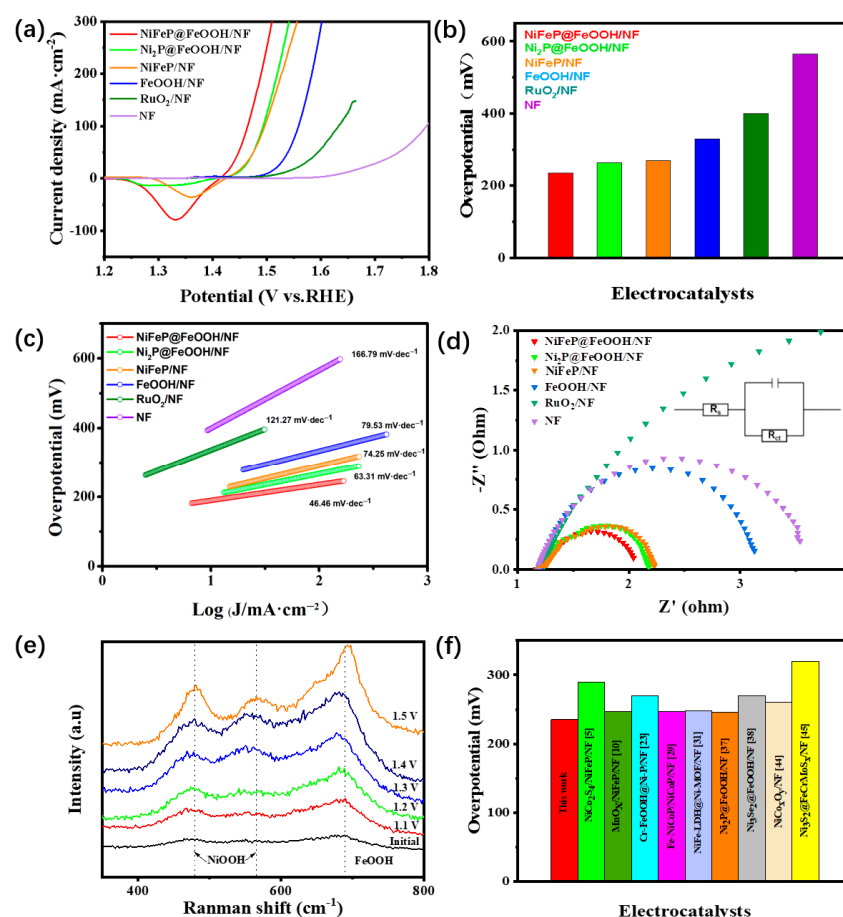

Figure 5. (**a**) OER LSV curves of NiFeP@FeOOH/NF, Ni$_2$P@FeOOH/NF, NiFeP/NF, FeOOH/NF, RuO$_2$/NF, and NF, (**b**) Bar chart of overpotential at corresponding current density of 100 mA cm^{-2}, (**c**) Corresponding tafel slope, (**d**) Corresponding Nyquist diagram, (**e**) In situ Raman spectra of NiFeP@FeOOH/NF and (**f**) Comparison bar chart of overpotential of different non-noble metal electrocatalysts at 100 mA cm^{-2}.

In Figure 6a,b, the electrochemical active surface area (ECSA) of the catalyst was determined using double-layer capacitance (C$_{dl}$) measurements in the Faradaic potential range. NiFeP@FeOOH/NF exhibits a C$_{dl}$ value of 4.13 mF cm^{-2}, which is high compared to NiFeP/NF (3.55 mF cm^{-2}), FeOOH/NF (0.20 mF cm^{-2}), and Ni$_2$P@FeOOH/NF

(2.20 mF cm^{-2}) (Figure S10). This implies that the addition of FeOOH and the formation of heterojunctions provide NiFeP@FeOOH/NF with more catalytic sites. Aside from its outstanding OER activity, NiFeP@FeOOH/NF's stability is a crucial component in practical applications. After 1000 CV cycles, the metal oxidation peak disappeared in the LSV curve of NiFeP@FeOOH/NF electrocatalyst compared with the initial, because the oxidation peak could be reduced or eliminated through multiple CV cycles, and the overpotential is still 235 mV (Figure 6c). The voltage variation trend of NiFeP@FeOOH/NF for 80 h at a steady current density of 50 mA cm^{-2} is shown in Figure 6d. It is stable for a significant amount of time at constant voltage because the voltage only slightly fluctuates over the course of 80 h. As clarified in Figure 6e, the LSV curve obtained after working for 80 h at a constant current density of 50 mA cm^{-2} rose slightly in comparison with the initial overpotential, which could be caused by the slight collapse of the nano-sheet structure on its surface in Figure S11. The XRD spectrum of the NiFeP@FeOOH/NF following the stability test is displayed in Figure S12. The XRD pattern did not change after the stability test, indicating that the composition of the material is stable. The XPS spectrum of the NiFeP@FeOOH/NF following the stability test is displayed in Figure S13. The peaks of Ni 2p and Fe 2p associated with Ni-P and Fe-P are observed to vanish, showing that the outer NiFeP@FeOOH is changed into nickel/iron hydroxide and oxide/hydroxyl oxide, which is caused by oxidation during oxygen evolution. A transmission analysis was performed on NiFeP@FeOOH after cycling, according to Figure S14, and it can be obviously observed that the heterogeneous nanosheet array is retained in the sample after cycling, but slight deformation occurred. In short, the electrocatalytic active phases of OER are nickel–iron hydroxide and nickel–iron oxide/hydroxyl oxide, respectively, which enrich the surface of NiFeP@FeOOH/NF.
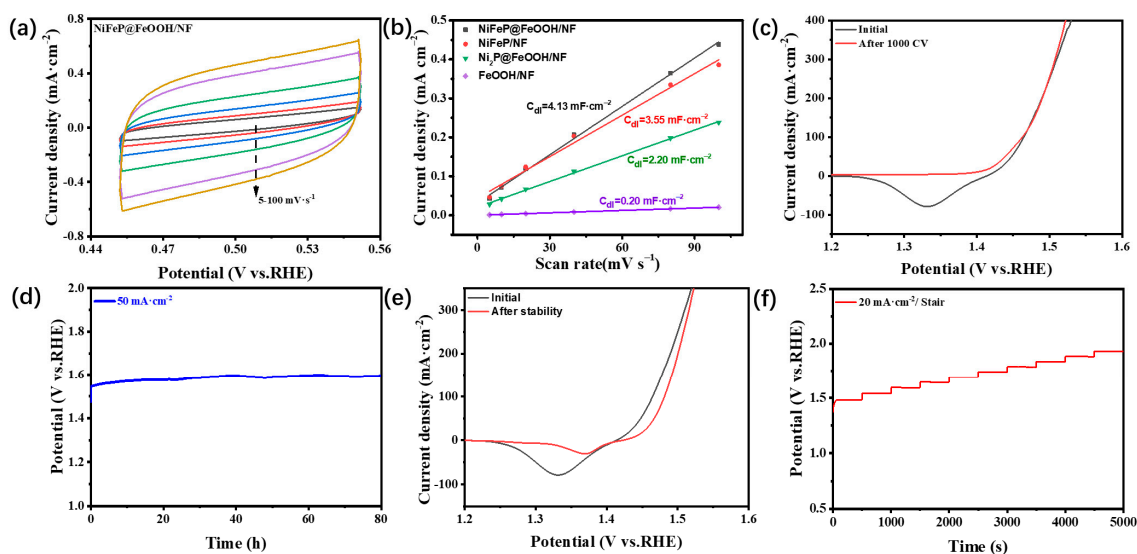

Figure 6. (**a**) ECSA of NiFeP@FeOOH/NF electrode measured by cyclic voltammograms at unequal scan velocities from 5 to 100 mV s^{-1}, (**b**) corresponding curve of current densities of NiFeP@FeOOH/NF, NiFeP/NF, Ni$_2$P@FeOOH/NF and FeOOH/NF as a function of scan velocity, (**c**) LSV for NiFeP@FeOOH/NF before and after 1000 cycles, (**d**) Long-term durability test, (**e**) LSV for NiFeP@FeOOH/NF initial and after long-term durability test 80 h, and (**f**) Multicurrent process of NiFeP@FeOOH/NF with an increment of 20 mA cm^{-2} per stair from 20 to 200 mA cm^{-2}.

Experiments with different KOH concentrations, temperatures, and the durability at different current densities were also carried out. As shown in Figure S15, NiFeP@FeOOH/NF requires overpotentials of 235 mV and 490 mV under a current density of 100 mA cm^{-2} in 1.0 M and 0.1 M KOH alkaline solutions. From Figure S16, it could be seen that NiFeP@FeOOH/NF requires overpotentials of 190 mV and 235 mV at 50 °C and 25 °C under a current density of 100 mA cm^{-2}. The result corresponds to higher reaction ac-

tivity and better performance at higher temperatures. The long-term durability test of NiFeP@FeOOH/NF at 50 and 100 mA cm^{-2} current densities is shown in Figure S17. NiFeP@FeOOH/NF could stably work for 80 h at a constant current density of 50 mA cm^{-2} as well as 57.5 h at 100 mA cm^{-2}. The result indicates that the stability is better with a lower current density.

3. Experimental

3.1. Chemicals

Nickel foam (NF) was purchased from Tianjin Damao Chemical Reagent Factory, China, and nickel nitrate hexahydrate (Ni(NO$_3$)$_2$·6H$_2$O), iron nitrate nonahydrate (Fe(NO$_3$)$_2$·9H$_2$O), ammonium fluoride (NH$_4$F), ferrous chloride tetrahydrate (FeCl$_2$·4H$_2$O) and urea CO(NH$_2$)$_2$ were obtained from China National Pharmaceutical Group Co., Ltd. Sodium hypophosphite (NaH$_2$PO$_2$) was provided by Tianjin FuChen Chemical Reagent Factory, China. All the compounds were analytically pure and did not require further handling.

3.2. Synthesis

3.2.1. Synthesis of NiFe Precursor/NF

In this research, the hydrothermal technique was used to create the bimetallic hydroxide complex of nickel hydroxide and iron hydroxide derived from nickel foam. The steps are as follows: First, 0.44 g Ni(NO$_3$)$_2$·6H$_2$O, 0.61 g Fe(NO$_3$)$_2$·9H$_2$O, 0.90 g CO(NH$_2$)$_2$ and 0.45 g NH$_4$F were added into 55 mL of distilled water. The solution was mixed evenly by a magnetic stirrer at normal temperature. The resulting solution was added to a reaction kettle containing NF (2 × 3 cm^2), which was put in an oven set at 120 °C for 12 h. After several washes to eliminate impurities, the generated NiFe precursor was vacuum dried.

3.2.2. Synthesis of NiFeP/NF

The dried NiFe precursor was placed downstream of the porcelain boat, and 0.5 g of sodium hypophosphite was weighed and placed on the other side of the boat. The porcelain boat was then placed in tube furnace at 350 °C for 3 h with a heating rate of 3 °C min^{-1}, naturally cooled to room temperature, removed, cleaned to remove impurities, and vacuum dried.

3.2.3. Synthesis of NiFeP@FeOOH/NF

The electrolyte of electrodeposition was a 0.1 M FeCl$_2$ solution. The sample was then electrodeposited for 100 s at a constant current density of 5 mA cm^{-2}, cleaned, and dried for 12 h at 60 °C. In this section, the samples produced via electrodeposition for 100 s are referred to as NiFeP@FeOOH/NF.

4. Conclusions

Through a hydrothermal reaction, phosphorization, and electrodeposition, we successfully constructed the heterostructure NiFeP@FeOOH nanosheets supported by NF. The resulting NiFeP@FeOOH/NF electrocatalyst exhibits favorable OER electrocatalytic activity, quick kinetics, and superior durability. While in 1.0 M KOH solution, NiFeP@FeOOH/NF has an overpotential of 235 mV at a current density of 100 mA cm^{-2}. The formation of the NiFeP@FeOOH heterostructure nanosheets on NF can decrease the resistance to contact between the catalyst and the base. After the addition of FeOOH, NiFeP@FeOOH/NF has a larger ECSA and more electroactive centers, and the synergistic effect among the multiple components can be realized. The addition of FeOOH can improve electrocatalytic activity by enhancing intermediate adsorption free energy and causing local electron redistribution. This project presents a fresh and creative approach for the rational design and advancement of catalyst interface engineering with a wide range of potential applications.

(a,b) SEM images of Ni_2P/NF; Figure S3: (a,b) SEM images of FeOOH/NF; Figure S4: SEM images of NiFe precursor at different hydrothermal temperatures (a) 50 °C, (b) 100 °C, (c) 120 °C, and (d) 150 °C; Figure S5: (a–d) HRTEM images of the NiFeP@FeOOH/NF; Figure S6: NiFeP@FeOOH/NF contact angle test; Figure S7: LSV of NiFe precursor, NiFeP/NF, and NiFeP@FeOOH/NF; Figure S8: NiFeP@FeOOH/NF LSV curves of different electrodeposition times; Figure S9: (a) NiFeP@FeOOH/NF electrodeposition of 125 s, (b) NiFeP@FeOOH/NF electrodeposition of 200 s; Figure S10: ECSA was measured by cyclic voltammetry at a scanning speed ranging from 5 mV s^{-1} to 100 mV s^{-1} (a) NiFe precursor, (b) NiFeP/NF, (c) FeOOH/NF, and (d) Ni2P@FeOOH/NF; Figure S11: (a) SEM image after stability test, (b) SEM image after 1000 CV cycle; Figure S12: XRD patterns of NiFeP@FeOOH/NF inital and after stability test high resolution High-resolution fitted; Figure S13: XPS spectra of NiFeP@FeOOH/NF after stability (a) Ni 2p, (b) Fe 2p, and (c) P 2p; Figure S14: (a,b) HRTEM images of the NiFeP@FeOOH/NF after 1000 CV cycle, (c) SAED image of NiFeP@FeOOH/NF after 1000 CV cycle; Figure S15: OER LSV curves of NiFeP@FeOOH/NF in 1.0 M and 0.1 M KOH alkaline solutions; Figure S16: OER LSV curves of NiFeP@FeOOH/NF at 50 °C and 25 °C in 1.0 M KOH alkaline solution; Figure S17: Long-term durability test of NiFeP@FeOOH/NF at 100 and 50 mA cm^{-2} current densities; Table S1: Comparison of binding energies of of NiFeP@FeOOH/NF and NiFeP/NF, Table S2: Comparison of overpotentials of different OER electrocatalysts at 100 mA cm^{-2} in 1.0 M KOH solution. Refs. [46–59] are cited in the Supplementary Materials.

Data Availability Statement: No new data were created or analyzed in this study. Data sharing is not applicable to this article.

Conflicts of Interest: The authors declare no conflict of interest.

References

1. Gono, P.; Pasquarello, A. High-performance NiOOH/FeOOH electrode for OER catalysis. *J. Chem. Phys.* **2021**, *154*, 024706. [CrossRef] [PubMed]
2. Sun, K.; Qian, Y.; Jiang, H.L. Metal-Organic frameworks for photocatalytic water splitting and CO_2 reduction. *Angew. Chem. Int. Ed.* **2023**, *135*, e202217565. [CrossRef]
3. Li, L.; Cao, X.; Huo, J.; Qu, J.; Chen, W.; Liu, C.; Zhao, Y.; Liu, H.; Wang, G. High valence metals engineering strategies of Fe/Co/Ni-based catalysts for boosted OER electrocatalysis. *J. Energy Chem.* **2023**, *76*, 195–213. [CrossRef]
4. Theerthagiri, J.; Lee, S.J.; Murthy, A.P.; Madhavan, J.; Choi, M.Y. Fundamental aspects and recent advances in transition metal nitrides as electrocatalysts for hydrogen evolution reaction: A review. *Curr. Opin. Solid State Mater. Sci.* **2020**, *24*, 100805. [CrossRef]
5. Jiang, J.; Li, F.; Su, H.; Gao, Y.; Li, N.; Ge, L. Flower-like $NiCo_2S_4$/NiFeP/NF composite material as an effective electrocatalyst with high overall water splitting performance. *Chin. Chem. Lett.* **2022**, *33*, 4367–4374. [CrossRef]
6. Li, L.; Guo, C.; Ning, J.; Zhong, Y.; Chen, D.; Hu, Y. Oxygen-vacancy-assisted construction of FeOOH/CdS heterostructure as an efficient bifunctional photocatalyst for CO_2 conversion and water oxidation. *Appl. Catal. B Environ.* **2021**, *293*, 120203. [CrossRef]
7. Shahzad, A.; Zulfiqar, F.; Nadeem, M.A. Cobalt containing bimetallic ZIFs and their derivatives as OER electrocatalysts: A critical review. *Coord. Chem. Rev.* **2023**, *477*, 214925. [CrossRef]
8. Zeng, F.; Mebrahtu, C.; Liao, L.; Beine, A.K.; Palkovits, R. Stability and deactivation of OER electrocatalysts: A review. *J. Energy Chem.* **2022**, *69*, 301–329. [CrossRef]
9. Wu, H.; Huang, Q.; Shi, Y.; Chang, J.; Lu, S. Electrocatalytic water splitting: Mechanism and electrocatalyst design. *Nano Res.* **2023**, *16*, 9142–9157. [CrossRef]
10. Wang, P.; Luo, Y.; Zhang, G.; Wu, M.; Chen, Z.; Sun, S.; Shi, Z. MnO_x-decorated nickel-iron phosphides nanosheets: Interface modifications for robust overall water splitting at ultra-high current densities. *Small* **2022**, *18*, e2105803. [CrossRef]

11. Song, J.; Wei, C.; Huang, Z.F.; Liu, C.; Zeng, L.; Wang, X.; Xu, Z.J. A review on fundamentals for designing oxygen evolution electrocatalysts. *Chem. Soc. Rev.* **2020**, *49*, 2196–2214. [CrossRef] [PubMed]

12. Zeng, T.; Meng, X.; Huang, H.; Zheng, L.; Chen, H.; Zhang, Y.; Yuan, W.; Zhang, L.Y. Controllable Synthesis of Web-Footed PdCu Nanosheets and Their Electrocatalytic Applications. *Small* **2022**, *18*, 2107623. [CrossRef] [PubMed]

13. Gao, F.; He, J.; Wang, H.; Lin, J.; Chen, R.; Yi, K.; Huang, F.; Lin, Z.; Wang, M. Te-mediated electro-driven oxygen evolution reaction. *Nano Res. Energy* **2022**, *1*, e9120029. [CrossRef]

14. Zheng, Z.; Wu, D.; Chen, G.; Zhang, N.; Wan, H.; Liu, X.; Ma, R. Microcrystallization and lattice contraction of NiFe LDHs for enhancing water electrocatalytic oxidation. *Carbon Energy* **2022**, *4*, 901–913. [CrossRef]

15. Wu, B.; Gong, S.; Lin, Y.; Li, T.; Chen, A.; Zhao, M.; Chen, L. A unique NiOOH@FeOOH heteroarchitecture for enhanced oxygen evolution in saline water. *Adv. Mater.* **2022**, *34*, 2108619. [CrossRef] [PubMed]

16. Jeong, S.; Mai, H.D.; Nam, K.H.; Park, C.M.; Jeon, K.J. Self-Healing Graphene-Templated Platinum–Nickel Oxide Heterostructures for Overall Water Splitting. *ACS Nano* **2022**, *16*, 930–938. [CrossRef] [PubMed]

17. Prabhu, P.; Jose, V.; Lee, J.M. Design Strategies for Development of TMD-Based Heterostructures in Electrochemical Energy Systems. *Matter* **2020**, *2*, 526–553. [CrossRef]

18. Zheng, X.; Yang, J.; Xu, Z.; Wang, Q.; Wu, J.; Zhang, E.; Dou, S.; Sun, W.; Wang, D.; Li, Y. Ru–Co Pair Sites Catalyst Boosts the Energetics for the Oxygen Evolution Reaction. *Angew. Chem. Int. Ed.* **2022**, *61*, e202205946. [CrossRef]

19. Wang, M.; Liu, X.; Wu, X. Realizing efficient electrochemical overall water electrolysis through hierarchical CoP@NiCo-LDH nanohybrids. *Nano Energy* **2023**, *114*, 108681. [CrossRef]

20. Park, S.; Kim, J.; Kwon, K. A review on biomass-derived N-doped carbons as electrocatalysts in electrochemical energy applications. *Chem. Eng. J.* **2022**, *446*, 137116. [CrossRef]

21. De, A.; Karmakar, A.; Kundu, S. Enhancing the Surface-Active Sites of Bimetallic 2D Hydroxide Materials by Introducing Fe^{2+} Ions toward Effective Hydroxide Adsorption for the Water Oxidation Reaction. *ACS Appl. Energy Mater.* **2023**, *6*, 5761–5773. [CrossRef]

22. Wang, D.; Umar, A.; Wu, X. Enhanced water electrolysis performance of bifunctional NiCoP electrocatalyst in alkaline media. *J. Electroanal. Chem.* **2023**, *950*, 117888. [CrossRef]

23. Xu, S.; Du, Y.; Yu, X.; Wang, Z.; Wang, X.; Cheng, X.; Liu, Q.; Luo, Y.; Suo, X.; Wu, Q. A Cr-FeOOH@Ni-P/NF binder-free elec-trode as an excellent oxygen evolution reaction electrocatalyst. *Nanoscale.* **2021**, *13*, 17003–17010. [CrossRef] [PubMed]

24. Li, Y.; Wu, Y.; Yuan, M.; Hao, H.; Lv, Z.; Xu, L.; Wei, B. Operando spectroscopies unveil interfacial FeOOH induced highly reactive β-Ni(Fe)OOH for efficient oxygen evolution. *Appl. Catal. B Environ.* **2022**, *318*, 121825. [CrossRef]

25. Wang, X.; Xiang, R.; Li, S.; Song, K.; Huang, W. Self-standing 2D/2D Co_3O_4@FeOOH nanosheet arrays as promising catalysts for the oxygen evolution reaction. *Dalton Trans.* **2023**, *52*, 2002–2012. [CrossRef] [PubMed]

26. Zhang, K.; Wang, F.; Li, X.; Wang, S.; Wang, Y.; Zha, Q.; Ni, Y. Connected design of Ni foam-supported porous Ni and FeOOH/porous Ni electrocatalysts for overall water splitting in alkaline media. *J. Alloy. Compd.* **2023**, *942*, 169014. [CrossRef]

27. Yu, J.; Wang, J.; Long, X.; Chen, L.; Cao, Q.; Wang, J.; Qiu, C.; Lim, J.; Yang, S. Formation of FeOOH nanosheets induces sub-stitutional doping of CeO_2-x with high-valence Ni for efficient water oxidation. *Adv. Energy Mater.* **2021**, *11*, 2002731. [CrossRef]

28. Dai, M.; Wang, R. Synthesis and Applications of Nanostructured Hollow Transition Metal Chalcogenides. *Small* **2021**, *17*, 2006813. [CrossRef]

29. Zhu, J.; Lu, Y.; Liu, C.; Cheng, T.; Xu, S.; Li, D.; Jiang, D. Template confined construction of Fe-NiCoP/NiCoP/NF hetero-structures for highly efficient electrocatalytic oxygen evolution reaction. *Int. J. Hydrogen Energy* **2021**, *46*, 37746–37756. [CrossRef]

30. Chowdhury, P.R.; Medhi, H.; Bhattacharyya, K.G.; Hussain, C.M. Recent progress in the design and functionalization strategies of transition metal-based layered double hydroxides for enhanced oxygen evolution reaction: A critical review. *Coord. Chem. Rev.* **2023**, *483*, 215083. [CrossRef]

31. Zeng, X.; Cai, Z.; Zhang, V.; Wang, D.; Xu, J.; Wang, X. Novel NiFe-LDH@Ni-MOF/NF heterostructured electrocatalysts for efficient oxygen evolution. *Mater. Res. Lett.* **2022**, *10*, 88–96. [CrossRef]

32. Jin, Y.; Zhang, M.; Song, L.; Zhang, M. Research Advances in Amorphous-Crystalline Heterostructures Toward Efficient Electrochemical Applications. *Small* **2022**, *19*, e2206081. [CrossRef]

33. Zhao, M.; Cheng, X.; Xiao, H.; Gao, J.; Xue, S.; Wang, X.; Wu, H.; Jia, J.; Yang, N. Cobalt-iron oxide/black phosphorus nanosheet heterostructure: Electrosynthesis and performance of (photo-)electrocatalytic oxygen evolution. *Nano Res.* **2022**, *16*, 6057–6066. [CrossRef]

34. Liang, H.; Gandi, A.; Xia, C.; Hedhili, M.; Anjum, D.; Schwingenschloogl, U.; Alshareef, H. Amorphous NiFe-OH/NiFeP electrocatalyst fabricated at low temperature for water oxidation applications. *ACS Energy Lett.* **2017**, *2*, 1035–10426. [CrossRef]

35. Feng, J.; Chen, M.; Zhou, P.; Liu, D.; Chen, Y.; He, B.; Bai, H.; Liu, D.; Ip, W.; Chen, D.; et al. Recon-struction optimization of distorted FeOOH/Ni hydroxide for enhanced oxygen evolution reaction. *Mater. Today Energy.* **2022**, *27*, 101005. [CrossRef]

36. Huang, C.; Qin, P.; Luo, Y.; Ruan, Q.; Liu, L.; Wu, Y.; Li, Q.; Xu, Y.; Liu, R.; Chu, P. Recent progress and perspective of cobalt-based catalysts for water splitting: Design and nanoarchitectonics. *Mater. Today Energy.* **2022**, *23*, 100911. [CrossRef]

37. Zhang, Y.; You, L.; Liu, Q.; Li, Y.; Li, T.; Xue, Z.; Li, G. Interfacial Charge Transfer in a Hierarchical Ni_2P/FeOOH Heterojunction Facilitates Electrocatalytic Oxygen Evolution. *ACS Appl. Mater. Interfaces* **2021**, *13*, 2765–2771. [CrossRef]

38. Gao, J.; Ma, H.; Zhang, L.; Luo, X.; Yu, L. Interface engineering of Ni$_3$Se$_2$@FeOOH heterostructure nanoforests for highly-efficient overall water splitting. *J. Alloys Compd.* **2022**, *893*, 162244. [CrossRef]

39. Li, S.; Li, M.; Ni, Y. Grass-like Ni/Cu nanosheet arrays grown on copper foam as efficient and non-precious catalyst for hydrogen evolution reaction. *Appl. Catal. B Environ.* **2019**, *268*, 118392. [CrossRef]

40. Luo, R.; Li, Y.; Xing, L.; Wang, N.; Zhong, R.; Qian, Z.; Du, C.; Yin, G.; Wang, Y.; Du, L. A dynamic Ni(OH)$_2$-NiOOH/NiFeP heterojunction enabling high-performance E-upgrading of hydroxymethylfurfural. *Appl. Catal. B Environ.* **2022**, *311*, 121357. [CrossRef]

41. Li, J.; Song, M.; Hu, Y.; Zhu, Y.; Zhang, J.; Wang, D. Hybrid heterostructure Ni$_3$N|NiFeP/FF self-supporting electrode for high-current-density alkaline water Electrolysis. *Small Methods* **2023**, *7*, e2201616. [CrossRef]

42. Chen, T.; Li, B.; Song, K.; Wang, C.; Ding, J.; Liu, E.; Chen, B.; He, F. Defect-activated surface reconstruction: Mechanism for triggering the oxygen evolution reaction activity of NiFe phosphide. *J. Mater. Chem. A* **2022**, *10*, 22750–22759. [CrossRef]

43. Zhu, T.; Han, J.; Sun, T.; Chen, J.; Wang, S.; Ren, S.; Pi, X.; Xu, J.; Chen, K. Interface-Enhanced SiO$_x$/Ru Heterocatalysts for Efficient Electrochemical Water Splitting. *ACS Appl. Mater. Interfaces* **2023**, *15*, 8200–8207. [CrossRef]

44. Guo, G.; Zhong, D.; Zhao, T.; Liu, G.; Li, J.; Zhao, Q. NiCo-BDC derived Co^{3+} enriched NiCo$_x$O$_y$/NF nanosheets for oxygen evolution reaction. *Int. J. Hydrogen Energy.* **2022**, *47*, 23094–23105. [CrossRef]

45. Zhang, Y.; Wang, S.; Zhong, H.; Ma, X.; Cao, Z. Morphology restructuring: MOFs derived Ni$_3$S$_2$@FeCrMoS$_x$/NF as a highly efficient and stable catalyst for water oxidation. *Int. J. Hydrogen Energy* **2023**, *48*, 1852–1862. [CrossRef]

46. Hao, H.; Li, Y.; Wu, Y.; Wang, Z.; Yuan, M.; Miao, J.; Lv, Z.; Xu, L.; Wei, B. *In-situ* probing the rapid reconstruction of FeOOH-decorated NiMoO$_4$ nanowires with boosted oxygen evolution activity. *Mater. Today Energy.* **2022**, *23*, 100887. [CrossRef]

47. Zhuang, S.; Tong, S.; Wang, H.; Xiong, H.; Gong, Y.; Tang, Y.; Liu, J.; Chen, Y.; Wan, P. The P/NiFe doped NiMoO$_4$ micro-pillars arrays for highly acreaction towards overall water splitting. *Int. J. Hydrogen Energy.* **2019**, *44*, 24546–24558. [CrossRef]

48. Shi, X.; Li, J.; Zhang, X.; Guo, J. MOF derived NiCo-LDH hollow structure for oxygen evolution reaction. *J. Phys. Chem. Solids.* **2023**, *172*, 11105. [CrossRef]

49. Guo, Z.; Wang, X.; Yang, F.; Liu, Z. Synergistic effect of Co and Fe bimetallic oxides/hydroxides composite structure as a bifunctional electrocatalyst for enhancing overall water splitting performance. *J. Alloys Compd.* **2022**, *895*, 162614. [CrossRef]

50. Liang, D.; Mao, J.; Liu, P.; Li, J.; Yan, J.; Song, W. In-situ doping of Co in nickel selenide nanoflower for robust electrocatalysis towards oxygen evolution. *Int. J. Hydrogen Energy.* **2020**, *45*, 27047–27055. [CrossRef]

51. Zhang, J.; Hou, K.; Yao, Q.; Wu, C.; Huang, M.; Guan, L. Heterogeneous Ni-Fe-P integrated with nickel foam as an efficient and durable electrocatalyst for water oxidation. *Int. J. Hydrogen Energy.* **2019**, *44*, 11684–11694. [CrossRef]

52. Bian, J.; Song, Z.; Li, X.; Zhang, Y.; Cheng, C. Nickel iron phosphide ultrathin nanosheets anchored on nitrogen-doped carbon nanoflake arrays as a bifunctional catalyst for efficient overall water splitting. *Nanoscale.* **2020**, *12*, 8443–8452. [CrossRef]

53. Read, C.G.; Callejas, J.F.; Holder, C.F.; Schaak, R.E. General Strategy for the Synthesis of transition metal phosphide films for electrocatalytic hydrogen and oxygen evolution. *ACS Appl. Mater. Interfaces.* **2016**, *8*, 12798–12803. [CrossRef]

54. Lin, J.; Yan, Y.; Li, C.; Si, X.; Wang, H.; Qi, J.; Cao, J.; Zhong, Z.; Fei, W.; Feng, J. Bifunctional electrocatalysts based on Mo-doped NiCoP nanosheet arrays for overall water splitting. *Nano-Micro Lett.* **2019**, *11*, 55. [CrossRef]

55. Lin, Y.; Pan, Y.; Liu, S.; Sun, K.; Cheng, Y.; Liu, M.; Wang, Z.; Li, X.; Zhang, J. Construction of multi-dimensional core/shell Ni/NiCoP nano-heterojunction for efficient electrocatalytic water splitting. *Appl. Catal. B Environ.* **2019**, *259*, 118039. [CrossRef]

56. Duan, J.; Chen, S.; Vasileff, A.; Qiao, S.Z. Anion and cation modulation in metal compounds for bifunctional overall water splitting. *ACS nano.* **2016**, *10*, 8738–8745. [CrossRef]

57. Dong, G.; Chen, T.; Xie, F.; Xue, D.; Liu, T.; Chen, L.; Xia, J.; Du, S.; Wang, F.; Xie, F.; et al. NiFeP composites supported on Ni foam as an efficient and robust bifunctional electrocatalyst for overall water splitting in alkaline solution. *J. Alloys Compd.* **2023**, *968*, 171764. [CrossRef]

58. Zhang, C.; Xie, Y.; Deng, H.; Zhang, C.; Su, J.W.; Dong, Y.; Lin, J. Ternary nickel iron phosphide supported on nickel foam as a high-efficiency electrocatalyst for overall water splitting. *Int. J. Hydrogen Energy.* **2018**, *43*, 7299–7306. [CrossRef]

59. Wang, X.D.; Chen, H.Y.; Xu, Y.F.; Liao, J.F.; Chen, B.X.; Rao, H.S.; Kuang, D.B.; Su, C.Y. Self-supported NiMoP$_2$ nanowires on carbon cloth as an efficient and durable electrocatalyst for overall water splitting. *J. Mater. Chem. A.* **2017**, *5*, 7191–7199. [CrossRef]